Silicon coupled-resonator optical-waveguide-based biosensors using light-scattering pattern recognition with pixelized mode-field-intensity distributions

Jiawei Wang, Zhanshi Yao, Ting Lei and Andrew W. Poon

Supplementary information

S1. Numerical calculations of coupling coefficient and effective refractive index values for transfer-matrix modeling

We model the imperfect CROWs using transfer-matrix method. We use as modeling parameters the numerically calculated values of coupling coefficient, κ, and effective refractive index, n_{eff}, from finite-element method (FEM) and two-dimensional (2D) finite-difference time-domain (FDTD) simulations. The waveguide dimensions of the microring CROWs considered in the simulations are based on the statistics of the measured waveguide widths and coupling gap widths from our SEM characterization (see section S2) of a representative fabricated CROW device. We assume a fixed waveguide height of 240 nm following the silicon layer thickness of the SOI wafer. We consider only the TM polarization.

Fig. S1(a) shows the numerically calculated linear relationship between the waveguide width of interest and n_{eff} (assuming a water upper-cladding with a refractive index of 1.318). Fig. S1(b) shows the numerically calculated linear relationship between the cladding refractive index of interest and n_{eff} (assuming a waveguide width of 470 nm). We use the relationship, $\Delta n_{eff}/\Delta n \sim 0.45$, shown in Fig. S1(b) to relate the change in effective refractive index, Δn_{eff}, used in the transfer-matrix modeling with the change in cladding refractive index, Δn.

Fig. S1(c) shows the FDTD-simulated electric mode-field amplitude profile of a coupling region (assuming a directional coupler with an interaction length of 3.5 μm, with no cavity enhancement), with a coupling gap width of 119 nm.

Fig. S1(d) shows the numerically calculated linear relationship between the coupling gap spacing and κ. We extract the κ values from the calculated electric mode-field amplitude profiles, as shown in Fig. S1(c). We note that κ increases with the coupling gap spacing because the designed interaction length of 3.5 μm slightly exceeds the coupling length of the directional coupler for a coupling gap spacing of 119 nm.

S2. Statistics of the measured waveguide widths and coupling gap widths

Figs. S2(a) and (b) show the statistics of the measured waveguide widths and coupling gap widths over one representative fabricated CROW device. We can approximately fit both distributions by Gaussian functions. The waveguide width, W_{wg}, shows a mean value of 469.9 ± 1.6 nm. The coupling gap width, W_{gap}, shows a mean value of 119.1 ± 1.3 nm. In both distributions, the uncertainties are given by the standard deviations. Figs. S2(c)-(k) show the zoom-in-view SEM images of all the nine coupling regions along the CROW counting from the input-port to the drop-port.

S3. Validity of the sensing algorithm using only the principal and second-principal components

We demonstrate by modeling that our sensing algorithm using only the ρ^p and ρ^s values can uniquely extract the Δn value for N up to at least 28. Here, we show our modeling results assuming N = 28. We assume a strong inter-cavity coupling, given by $\kappa = 0.910 \pm 0.004$, and an effective refractive index, given by $n_{eff} = 1.839 \pm 0.002$, following the same statistics detailed in section S2. We assume a waveguide loss of 2.2 dB/cm. Fig. S3(a) shows the modeled transmission spectra of an imperfect 28-element microring CROW. Fig. S3(b) shows the 28 modeled eigenstate pixelized patterns. Fig. S3(c) shows the calculated $\{\rho_j'(\lambda_0)\}$ as a function of Δn, with $\Delta n_d = 6.204\times10^{-2}$ RIU and $\Delta n_i = 1.2\times10^{-4}$ RIU. Fig. S3(d) shows the calculated differential correlation coefficients per unit Δn, given as $(d(\rho'(\lambda_0))/d(\Delta n))$. Fig. S3(e) shows the modeled sensitivity as a function of λ_p. The sensitivity spans a range from12 RIU^{-1} to 1664 RIU^{-1} over the spectral 3dB-bandwidth, with an average sensitivity of ~370 RIU^{-1}.

We arbitrarily choose a fixed probe wavelength λ_p at 1558.18 nm (Fig. S3(a)). Fig. S4 illustrates the sensing scheme using the correlation analysis. Fig. S4(a) shows the modeled pixelized patterns at λ_p without (buffer) and with (test) applying a Δn that is arbitrarily chosen as 1.80×10^{-3} RIU. Fig. S4(b) shows the two sets of modeled correlation coefficients of the two pixelized patterns without and with Δn. The ρ^p and ρ^s without Δn are ρ_8 and ρ_{12}, respectively. The ρ^p and ρ^s with Δn are ρ_8 and ρ_{27}, respectively. Fig. S4(c) shows the calculated library of ρ_8' and ρ_{12}' as a function of Δn and mapping of ρ_8 and ρ_{12} values for the buffer to the library. Fig. S4(d) shows the calculated library of ρ_8' and ρ_{27}' as a function of Δn and mapping of ρ_8 and ρ_{27} values for the test to the library . We extract from the library a $\Delta n = \Delta n_{B'} - \Delta n_B = 1.80\times10^{-3}$ RIU, which agrees with the chosen Δn value.

S4. Correcting the measured pixelized patterns against surface-roughness-induced modulations

The as-measured pixelized patterns are prone to be distorted by the non-uniform surface-roughness-induced scattering. In order to correct for such an image distortion, we normalize the measured pixelized patterns with estimated surface-roughness-induced modulations. We estimate the modulations by calculating the root-mean-square (RMS) value for each integration window in a pixelized pattern. The extracted RMS value is normalized to the integrated intensity value of each pixel. Fig. S5(a) shows the as-measured pixelized eigenstate patterns. Fig. S5(b) shows the estimated intensity-normalized RMS distributions for the eigenstate patterns. Fig. S5(c) shows the corrected pixelized eigenstate patterns, as shown in Fig. 5(c) in the main article.

S5. Calibrated spectral sensitivity of the CROW sensor

We calibrate the spectral sensitivity of the CROW sensor in the spectral domain using NaCl solutions with known mass concentrations (from 1% to 5%, with a step of 1%) covering the CROW device surface. Fig. S6 shows the measured linear relationship between the transmission band spectral shifts and the Δn values upon different concentrations. The linear fit indicates a ~0.19nm spectral redshift per 1% concentration increment. For NaCl solutions of 1% to 10% concentrations, the refractive index change in the 1550nm wavelength range is known to be 0.0018 RIU per 1%[1]. Therefore, the CROW sensor exhibits a spectral sensitivity of ~106.82 nm/RIU in 1550 nm.

S6. Sensing performance comparison with waveguide- and microresonator-based refractive-index sensors in the spectral domain

We first compare the sensing performances of our CROW sensor with traditional waveguide-based refractive index sensors. Table S1 summarizes the performances of recently demonstrated on-chip waveguide-based refractive index sensors. We use a waveguide-based sensor without cavity resonant enhancement as a baseline device for sensitivity comparison. Usually, such a sensor works in a Mach-Zehnder interferometer (MZI) configuration. The sensitivity is given as[2]

$$S_{MZI} = \frac{L_s}{\lambda}\frac{\Delta n_{eff}}{\Delta n} \quad (2\pi \text{ RIU}^{-1}) \qquad (1)$$

where Δn_{eff} is the change in effective refractive index, Δn is the cladding refractive index change, L_s is the length of the sensing waveguide, and λ is the wavelength in vacuum.

Assuming the same waveguide dimension design in the TM mode as we adopted for the CROW sensor, and the same ratio of $\Delta n_{eff}/\Delta n \sim 0.45$ (see section S1), we compare the theoretically calculated sensitivity of the MZI

sensor defined in equation (1) with the modeled sensitivity of the CROW sensor (given by the larger differential correlation coefficient between $\rho'^{p}(\lambda_p)$ and $\rho'^{s}(\lambda_p)$). For a MZI sensor with the same sensing waveguide length as our designed 8-ring CROW total circumference length (~382.7 μm), the calculated sensitivity is ~110 (2π RIU^{-1}). This value falls with the range of the modeled sensitivity values of the CROW sensor (~1.6 - ~715 RIU^{-1}).

We also benchmark with the experimentally demonstrated sensitivity values from previous works using waveguide-based sensors in the MZI configuration[3,4]. Specifically, previous works using a spiral sensing waveguide with a few-mm length in a singlemode[3] or slot-mode[4] waveguide configuration have demonstrated sensitivity values of ~460 (2π RIU^{-1}) and ~932 (2π RIU^{-1}), respectively. Both are comparable to the average sensitivity of ~199 RIU^{-1} and the peak sensitivity of ~1412 RIU^{-1}demonstrated in this work.

For microresonator-based sensors in the spectral domain, the sensitivity is defined as an absolute value of the resonance wavelength shift corresponding to the cladding refractive index change[5-10]. We caution that it cannot be directly compared with the sensitivity defined for the CROW sensor in the spatial domain. Instead, it is possible to benchmark on the detection limit. Previous works on microresonator-based sensors in the spectral domain using various material platforms[5-10] have shown a detection limit down to ~10^{-4} – ~10^{-7} RIU. Our demonstrated NEDL at ~6×10^{-6} RIU at a specific probe wavelength is thus within the detection limit demonstrated by microresonator-based sensors in the spectral domain.

S7. Optimizing the CROW sensitivity

We investigate the sensitivity of the imperfect CROW sensors as a function of different device parameters, including the waveguide propagation loss α, the number of coupled cavities N, and the inter-cavity coupling coefficient κ based on the transfer-matrix modeling. We fix the same cavity circumference (47.8 μm) following our experiments and assume that the same degree of imperfection can be generally applied.

S7.1 Optimizing the sensitivity by tuning the waveguide propagation loss

Here we first show two specific cases of different waveguide losses assuming N = 16. Figs. S7(a)-(e) show the modeling results assuming a waveguide propagation loss of 22 dB/cm following our experiments. Figs. S8(a)-(e) show the modeling results assuming a waveguide propagation loss of 2.2 dB/cm following the typical SOI waveguide loss value reported in the literature[11,12].

Fig. S7(a) shows the modeled transmission spectra with 16 eigenstates. Fig. S7(b) shows the modeled 16 distinguishable eigenstate pixelized patterns. Figs. S7(c) and (d) show the modeled library of $\{\rho_j'(\lambda_0)\}$ as a function of Δn, and the calculated differential correlation coefficients per unit Δn, given as $(d(\rho_j'(\lambda_0))/d(\Delta n))$. Fig. S7(e) shows the extracted sensitivity as a function of λ_p. We observe an overall improved sensitivity compared to an 8-element CROW, with an average sensitivity of ~307 RIU^{-1}.

Fig. S8(a) shows the modeled transmission spectra with 16 eigenstates, assuming a reduced waveguide loss. Fig. S8(b) shows the modeled 16 distinguishable eigenstate pixelized patterns. Figs. S8(c) and (d) show the modeled library of $\{\rho_j'(\lambda_0)\}$ as a function of Δn and the calculated differential correlation coefficients per unit Δn, given as $(d(\rho_j'(\lambda_0))/d(\Delta n))$. Fig. S8(e) shows the extracted sensitivity as a function of λ_p. We observe an overall improvement sensitivity with an average sensitivity of ~375 RIU^{-1}, compared to the above case upon a 22dB/cm waveguide loss. This suggests that the sensitivity increases with a reduced α.

S7.2 Optimizing the sensitivity by tuning the number of coupled cavities

We systematically study the sensitivity as a function of N, assuming $\kappa \sim 0.91$ and $\alpha = 2.2$ dB/cm. We examine from 4 to 28, following the same procedures as above. For each CROW, we obtain an average sensitivity over the entire transmission band. For each N, we repeat the calculation 200 times by generating different device parameters following section S2. We obtain from the randomly generated devices 200 average sensitivity values, and the mean value and the uncertainty out of the 200 devices. Our modeling results indicate that the sensitivity of the imperfect CROW sensor increases with N before saturation and then rolls off. Fig. S9(a) shows that the average sensitivity reaches the optimized value of ~364 RIU^{-1} for N = 16. Therefore, the sensitivity can be optimized by increasing N to reach a saturation value.

S7.3 Optimizing the sensitivity by tuning the inter-cavity coupling coefficients

We studied the sensitivity as a function of κ, assuming N = 8 and $\alpha = 2.2$ dB/cm. We examine κ from 0.3 to 0.9. Our modeling results indicate that the sensitivity of the imperfect CROW sensor drops with increasing κ. Fig. S9(b) shows that the average sensitivity reaches the maximum value of ~633 RIU^{-1} at $\kappa \approx 0.3$, with a reduced $\Delta n_d \approx 1.7\times10^{-2}$ RIU.

Given a low waveguide propagation loss (2.2dB/cm) and a low coupling coefficient (~0.3), we further studied the optimized sensitivity as a function of N. The modeling results in Fig. S9(c) reveal an optimized average sensitivity of ~641 RIU^{-1} at N = 12.

References

1 Lide, D. R. CRC Handbook of Chemistry and Physics 2005 [Lide, D. R. (ed.)] [1308] (CRC Press, Boca Raton, 2005).

2 Schmid, J. et al. Silicon-on-insulator guided mode resonant grating for evanescent field molecular sensing *Opt. Express,* **17**, 18371-18380 (2009).

3 Densmore, A. et al. Spiral-path high-sensitivity silicon photonic wire molecular sensor with temperature independent response. *Opt. Lett.* **33**, 596-598 (2008).

4 Liu, Q. et al. Highly sensitive Mach–Zehnder interferometer biosensor based on silicon nitride slot waveguide. *Sensor Actuat. B - Chem.* **188**, 681-688 (2013).

5 Iqbal, M. et al. Label-free biosensor arrays based on silicon ring resonators and high-speed optical scanning instrumentation. *IEEE J. Sel. Top. Quant. Electron.* **16**, 654-661 (2010).

6 Barrios, C. A. et al. Slot-waveguide biochemical sensor. *Opt. Lett.* **32**, 3080-3082 (2007).

7 Claes, T. et al. Label-free biosensing with a slot-waveguide-based ring resonator in silicon on insulator. *IEEE Photon J.* **1**, 197-204 (2009).

8 Zamora, V., Lützow, P., Weiland, M. & Pergande, D. Investigation of cascaded SiN microring resonators at 1.3 µm and 1.5 µm. *Opt. Express* **21**, 27550-27557 (2013).

9 Hu, J. et al. Planar waveguide-coupled, high-index-contrast, high Q resonators in chalcogenide glass for sensing. *Opt. Lett.* **33**, 2500-2502 (2008).

10 Stern, L., Goykhman, I., Desiatov, B. & Levy, U. Frequency locked micro disk resonator for real time and precise monitoring of refractive index. *Opt. Lett.* **37**, 1313-1315 (2012).

11 Selvaraja, S. K. et al., Highly uniform and low-loss passive silicon photonics devices using a 300mm CMOS platform. Paper presented at Optical Fiber Communication Conference, San Francisco, California United States. Washington, DC United States: OSA Technical Digest. (2014, March 9-13)

12 OpSIS-IME, [Online]. Available: http://www.opsisfoundry.org

Tables and Figures for Supplementary Information

Table S1: Summary of on-chip optical waveguide- and microresonator-based refractive-index sensor performances

Configuration	Material	Length/ Cavity length (μm)	Q-factor	Sensitivity (RIU^{-1})	Detection limit (RIU)	Ref	Year
MZI with spiral waveguide	SOI	2000	NA	460 (2π)	1.1×10^{-5}	3	2008
MZI with slot-mode waveguide	SiN	7000	NA	932 (2π)	5.4×10^{-6}	4	2013
Microring	SOI	~ 94	4.3×10^{4}	163 nm	-	5	2010
Microring with slot-waveguide	Si_3N_4	~ 430	1800	212 nm	2.3×10^{-4}	6	2007
Microring with slot-waveguide	SOI	~41	~450	298 nm	4.2×10^{-5}	7	2009
Cascaded rings with Vernier scale	SiN	~3700 (2 rings)	10^{4}	9804 nm	2.04×10^{-6}	8	2013
Microdisk	Chalco-genide Glass	~126	2×10^{5}	182 nm	8×10^{-7}	9	2008
Microdisk	SiN	~188	10^{4}	-	10^{-7}	10	2012
CROW in the spatial domain (This work)	SOI	~382 (8 rings)	~914 - ~2176 (8 eigenstates)	5 - 1412	~9×10^{-4}- ~2×10^{-7} (~ 6×10^{-6} at 1565.56 nm)	-	2014

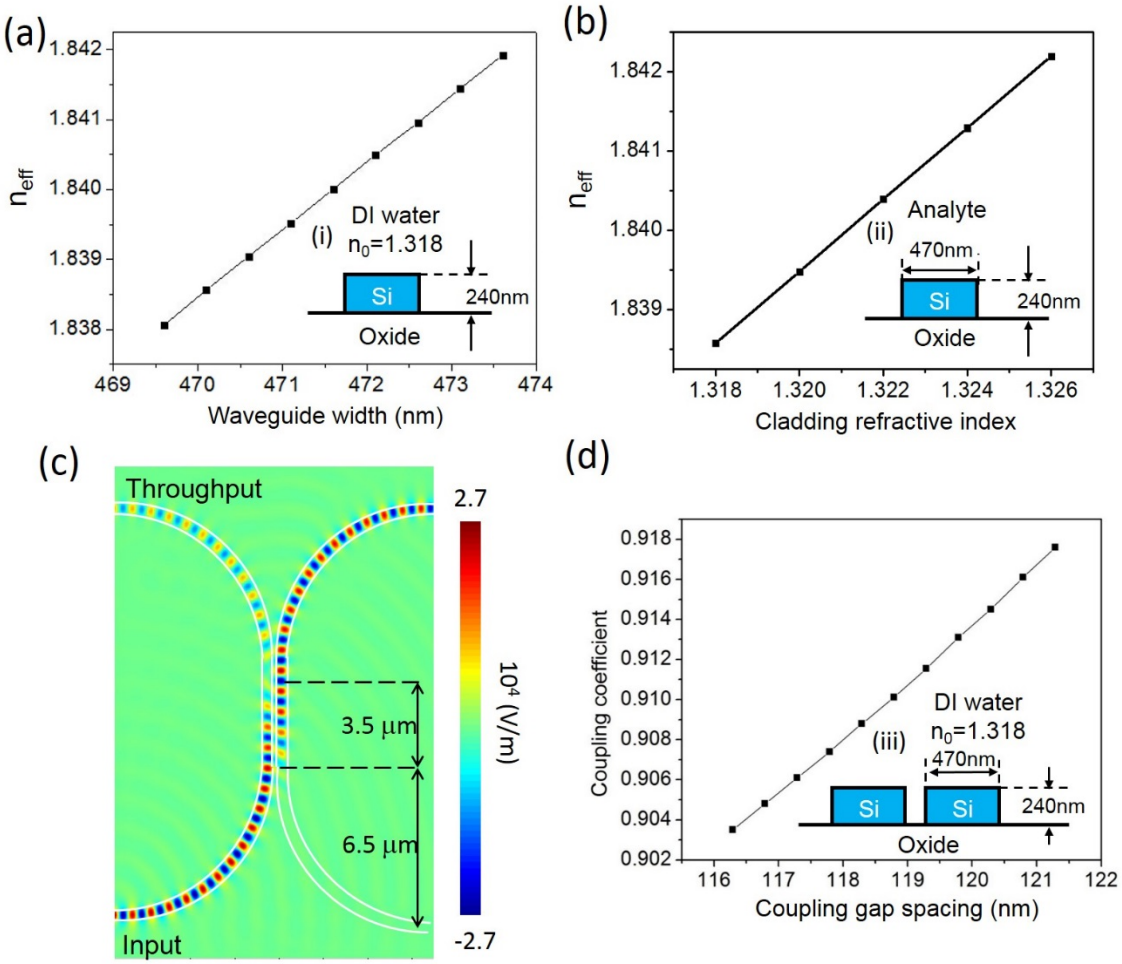

Fig. S1 (a) Simulated relationship between the waveguide width and n_{eff}. (b) Simulated relationship between the cladding refractive index and n_{eff}. (c) Simulated electric mode-field amplitude profile of a coupling region with a coupling gap width of 119 nm. (d) Simulated relationship between the coupling gap width and the coupling coefficient. Insets (i)-(iii): Schematics of the waveguide cross-sectional views for the simulations in (a), (b), (d), respectively.

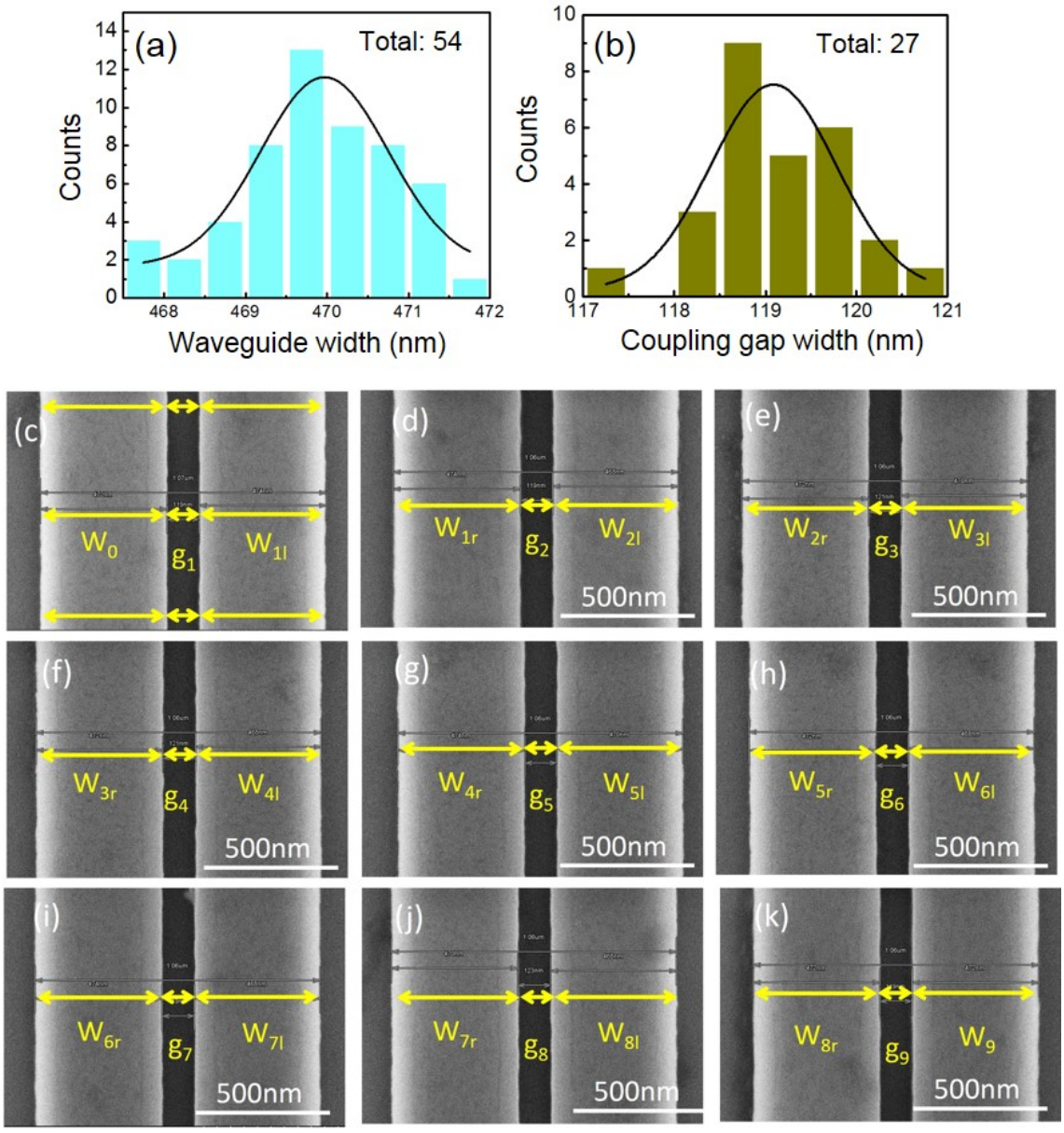

Fig. S2 (a)-(b) Statistics of the measured waveguide widths with a Gaussian fit. (b) Statistics of the measured coupling gap widths with a Gaussian fit. (c)-(k) Representative SEM images in the nine coupling regions of an imperfect CROW. The three sets of yellow arrows indicate where we obtain the three sets of waveguide widths and gap widths in a coupling region. Number 1 – 8 in the subscript of "W" denotes the ring cavity number (counting from the input side). Number 1 – 9 in the subscript of "g" denotes the gap spacing number (counting from the input side). The "*l*" and "r" in the subscript of "W" denote the width measurement at the left and right waveguide of the microring, respectively.

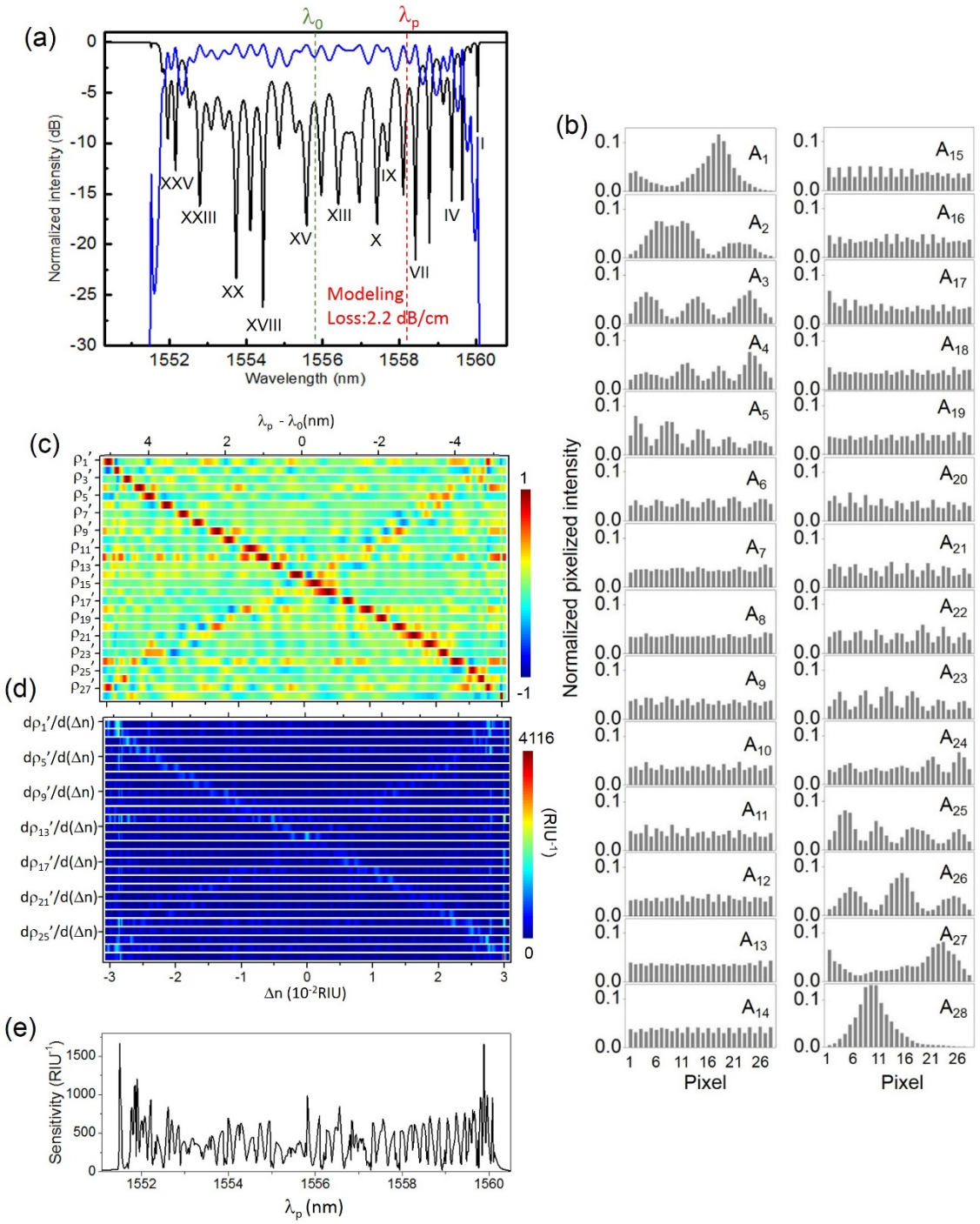

Fig. S3 (a) Modeled throughput- and drop-port transmission spectra of an imperfect 28-ring CROW. Green dashed line: reference wavelength λ_0 of 1555.82 nm. Red dashed line: probe wavelength λ_p of 1558.18 nm. (b) Modeled pixelized intensity patterns at eigenstates I - XXVIII. (c) Calculated library of the correlation coefficients ρ_1'- ρ_{28}' as a function of Δn at λ_0. (d) Calculated library of differential correlation coefficients as a function of Δn. (e) Calculated sensitivity as a function of λ_p.

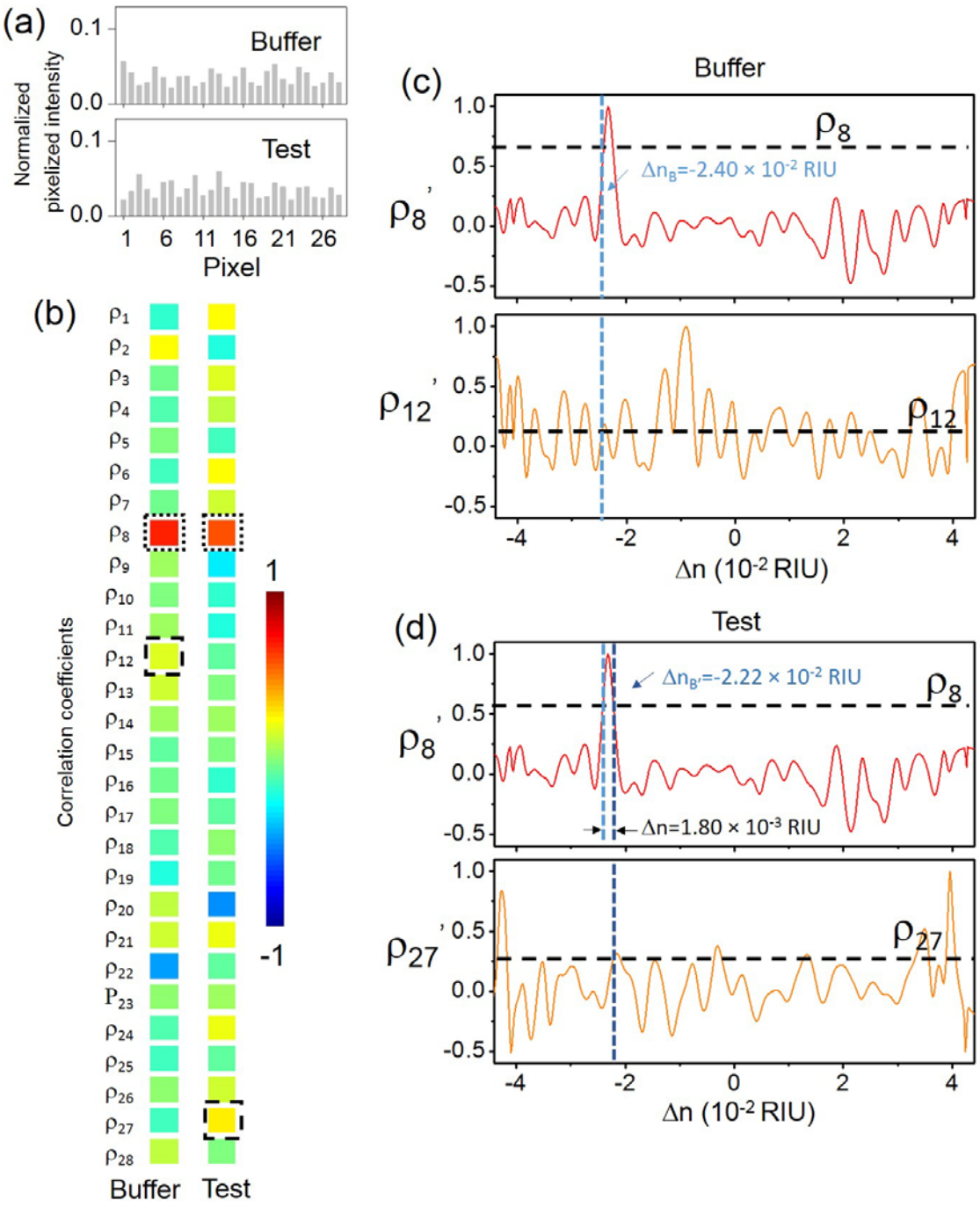

Fig. S4 (a) Modeled pixelized patterns at probe wavelength λ_p (1558.18nm) upon the buffer solution and the test solution. (b) Calculated sets of correlation coefficients upon the buffer solution and the test solution. The dotted-line boxes indicate ρ^p and the dashed-line boxes indicate ρ^s. (c) The calibrated ρ_8' and ρ_{12}' as a function of Δn and mapping of ρ_8 and ρ_{12} values to extract Δn_B. (d) The calibrated ρ_8' and ρ_{27}' as a function of Δn and mapping of ρ_8 and ρ_{27} values to extract Δn_B'.

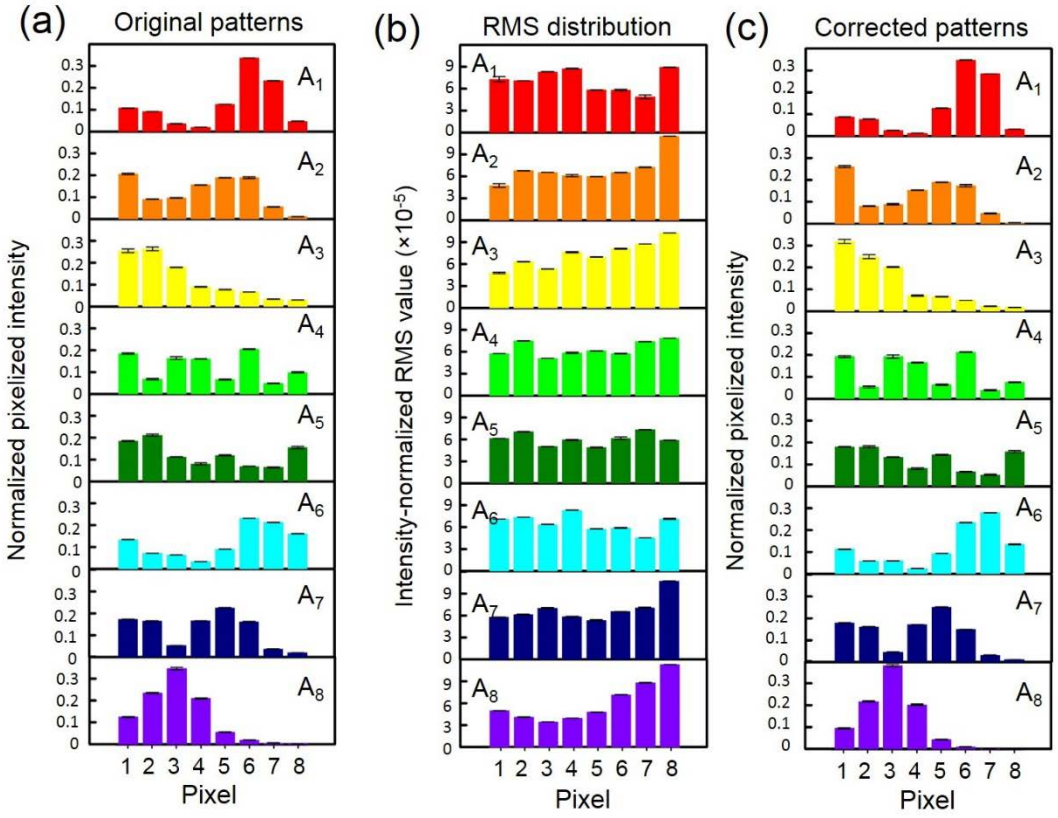

Fig. S5 (a) As-measured pixelized eigenstate patterns. (b) Intensity-normalized RMS distributions for the eigenstates I-VIII. (c) Corrected pixelized eigenstate patterns, same as Fig. 5 (c) in the main article.

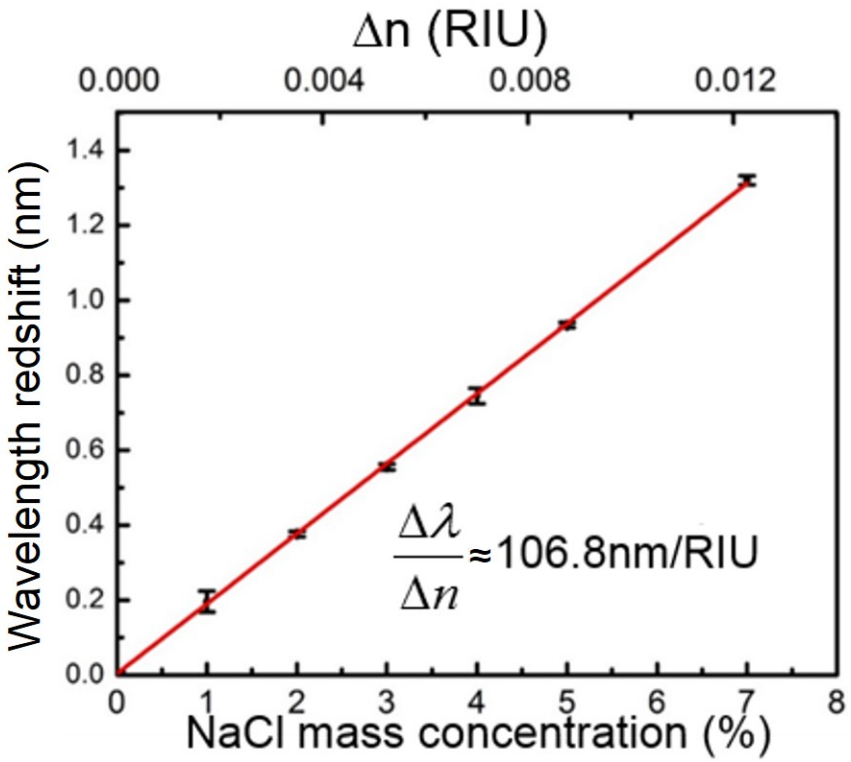

Fig. S6 Measured and fitted linear relationship between the resonance wavelength shifts and the refractive index change in the cladding layer with various NaCl mass concentrations.

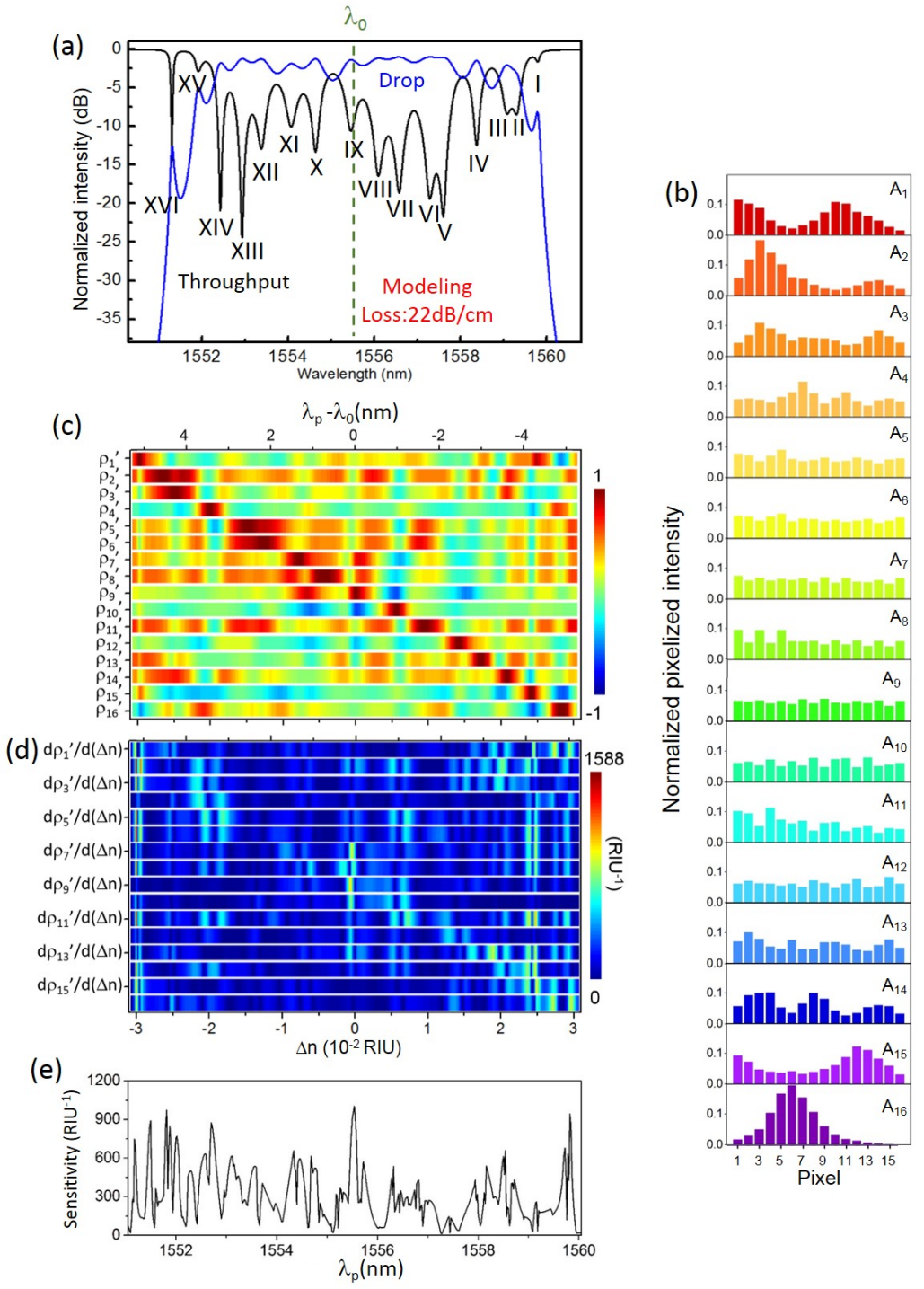

Fig. S7 (a) Modeled throughput- and drop-port transmission spectra of an imperfect 16-ring CROW assuming a waveguide loss of 22 dB/cm. Green dashed line: reference wavelength λ_0 of 1555.54 nm. (b) Modeled pixelized intensity patterns at eigenstates I-XVI. (c) Calculated library of the correlation coefficients ρ_1'-ρ_{16}' as a function of Δn at a fixed reference wavelength λ_0. (d) Calculated library of differential correlation coefficients as a function of Δn. (e) Calculated sensitivity as a function of λ_p.

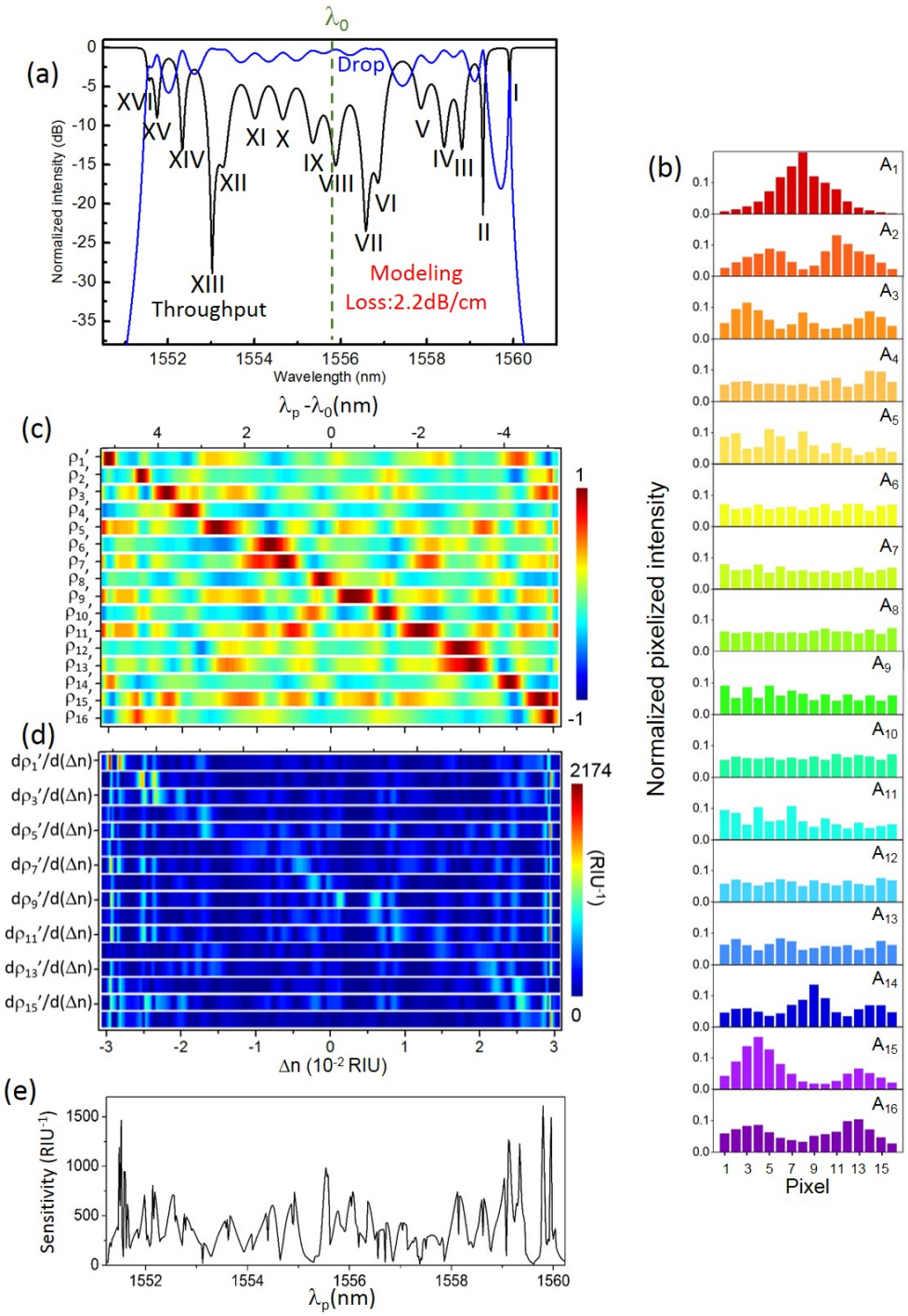

Fig. S8 (a) Modeled throughput- and drop-port transmission spectra of an imperfect 16-ring CROW assuming a waveguide loss of 2.2dB/cm. Green dashed line: reference wavelength λ_0 of 1555.74 nm. (b) Modeled pixelized intensity patterns at eigenstates I-XVI. (c) Calculated library of the correlation coefficients ρ_1'-ρ_{16}' as a function of Δn at a fixed reference wavelength λ_0. (d) Calculated library of differential correlation coefficients as a function of Δn. (e) Calculated sensitivity as a function of λ_p.

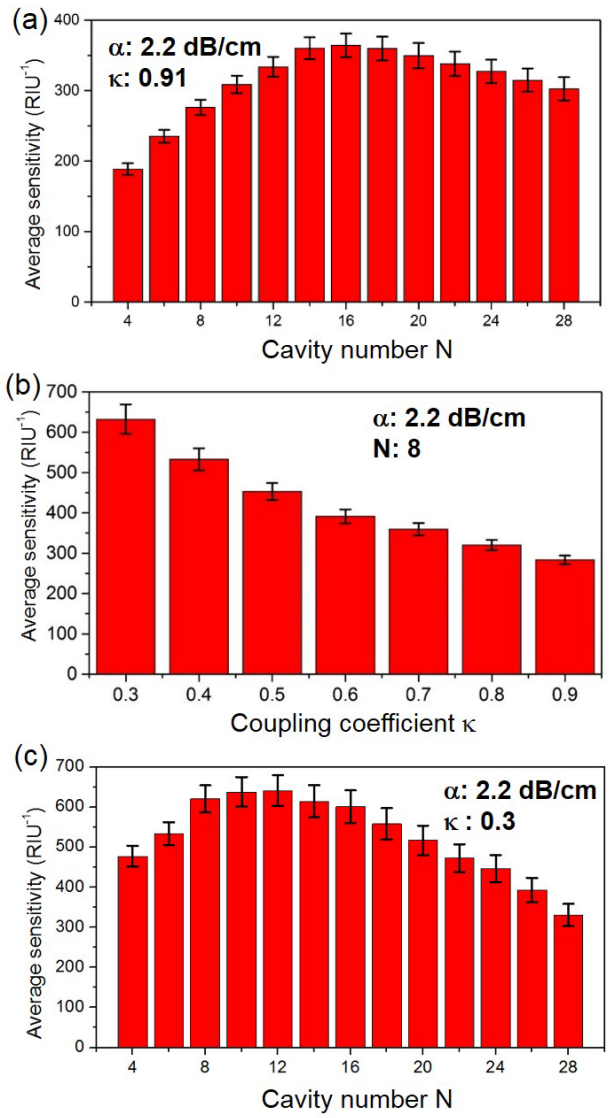

Fig. S9 (a) Modeled average sensitivity of the CROW as a function of cavity number assuming a coupling coefficient ~0.91 and a waveguide propagation loss of 2.2 dB/cm. (b) Modeled average sensitivity of the CROW as a function of coupling coefficient assuming a cavity number of 8 and a waveguide loss of 2.2 dB/cm. (c) Modeled average sensitivity of the CROW as a function of cavity number assuming a coupling coefficient ~0.3 and a waveguide loss of 2.2 dB/cm.